

Saliency-based variational active contour model for image with intensity inhomogeneity

Muhammad Syukri Mazlin¹, Abdul Kadir Jumaat^{1,2}, Rohana Embong¹

¹School of Mathematical Sciences, College of Computing, Informatics and Mathematics, Universiti Teknologi MARA, Shah Alam, Malaysia

²Institute for Big Data Analytics and Artificial Intelligence (IBDAAI), Universiti Teknologi MARA, Shah Alam, Malaysia

Article Info

Article history:

Received Feb 14, 2023

Revised Jul 13, 2023

Accepted Jul 16, 2023

Keywords:

Active contour

Intensity inhomogeneous image

Saliency image map

Selective image segmentation

Variational level set

ABSTRACT

Variational active contour model (ACM) is used to segment or subdivide an image into the desired object. This segmentation technique in region-based ACM can be divided into two classes: global segmentation and selective segmentation. Selective segmentation, in which only a particular desired object is segmented from an input image, is preferable to the global model because the selective segmentation model proves to be very useful, especially in medical image analysis. However, when it comes to segmenting an image with inhomogeneous intensity, these models seem to give unsatisfactory results. In this paper, we propose a new variational selective ACM mainly used for segmentation of images with inhomogeneous intensity, by incorporating saliency image map and local image fitting ideas. In addition, the euler-lagrange equation (EL) was provided to solve the proposed model. A total of thirty sets of medical images were used to test the model. Numerical results show that the suggested model outperforms other existing models, with the hausdorff distance of the proposed model being 47.78% less than the competing model, and the dice and jaccard values being around 17.54% and 33.65% higher, respectively, than the competing model.

This is an open access article under the [CC BY-SA](https://creativecommons.org/licenses/by-sa/4.0/) license.



Corresponding Author:

Abdul Kadir Jumaat

Institute for Big Data Analytics and Artificial Intelligence (IBDAAI), Universiti Teknologi MARA

Kompleks Al-Khawarizmi, 40450 Shah Alam, Selangor, Malaysia

Email: abdulkadir@tmsk.uitm.edu.my

1. INTRODUCTION

Image segmentation which is a process of dividing a digital image into various parts for subsequent processing and analysis is a crucial step in many image processing and computer vision applications, including medical imaging [1] and object recognition [2]–[5]. There are two types of segmentation methods: variational and non-variational segmentation methods. The non-variational approaches such as thresholding and region growing methods although effective for a simple image are not effective to handle topological changes, while the non-variational machine learning-based method required a large amount of data which is not usually available. Variational approaches are less dependent on the amount of data and have been proven to be effective in image segmentation. The active contour models (ACM) are the widely used method in variational approaches as they use the calculus of variations where it applies the optimization procedures to minimize the energy cost functional. The variational ACM can be categorized into two types which are edge-based and region-based approaches. The most celebrated edge-based variational ACM was proposed by Kass *et al.* [6] by applying the explicit snake model with a conventional parametric curve. However, this method is sensitive to image noise. Meanwhile, the region-based variational ACM uses image information such as the shape, texture characteristics and pixel intensities in global or local areas to properly converge contour curves to

acceptable target borders [7]–[9]. The region-based variational ACM approach is less sensitive to image noise and capable to handle topological changes more effectively compared to the edge-based approach. This region-based variational ACM can be classified into two classes which are global and selective segmentation.

The well-known variational global ACM is Mumford and Shah [10] model. As a global model, it aims to segment all objects that appear in the input image. Then, Chan and Vese [11] reduced the Mumford and Shah [10] model to a simple numerical representation without approximation called as chan-veese (CV) model. There are two phases in this CV model, depicting the image's background and foreground, which is a special case of the piecewise constant (PC) model. However, this CV model might produce unsatisfactory results. The main reason is that this model applied global image intensity information in its mathematical formulation which makes this model unable to produce prominent results when it comes to segmenting intensity inhomogeneity images. Intensity inhomogeneity is one of the main constraints in the field of image segmentation particularly in medical imaging such as magnetic resonance imaging (MRI) and computed tomography (CT) scans. This refers to variations in image intensity values within a single image, which can lead to difficulty in differentiating between healthy and diseased tissue which leads to the medical experts making inaccurate decisions. This is particularly problematic in diseases such as cancer, where accurate diagnosis is critical for effective treatment planning.

In order to overcome the problem of segmenting an intensity inhomogeneity image, Li *et al.* [12] have introduced the local binary fitting (LBF) model that utilizes the local image intensity. In conjunction with the good segmentation result in applying the LBF model, it increases the computational time due to the computational complexity in its formulation. Then in 2010, Zhang *et al.* [13] proposed the local image fitting (LIF) model to overcome the limitation of the LBF model. Since then, many researchers have utilized the local image intensity idea in image segmentation to deal with images with intensity inhomogeneity such as Wang and Huang [14], Yang *et al.* [15] and Iqbal *et al.* [16]. Besides the idea of using the local image intensity to obtain better image segmentation results for images with intensity inhomogeneity, another approach that is currently being noticeable by researchers is to use the saliency map idea. In general, saliency means the quality of being conspicuous by emphasizing the region to which people will look first. According to Zhi and Shen [17], the saliency map originates from visual distinctness and surprise. In other words, this saliency map will help in making its initial contour of the targeted object as its initial guess can easily extract the desired object from the background. Several studies have applied the saliency map idea in their models. One of the studies has been done by Idris *et al.* [18] namely the saliency driven region-edge based top down level set evolution (SDREL) where they have proven that the idea of using the saliency map can achieve a better and more precise segmentation result. However, Iqbal *et al.* [16] have claimed that the above-mentioned model is not efficient in segmenting an image with severe intensity inhomogeneity. Therefore, they came up with a new segmentation model called the local saliency fitting (LSF) by incorporating the same saliency images map in the SDREL model [18] with the local image intensity idea. Unfortunately, the LSF model is not applicable when segmenting a specific object in an input image.

To overcome this problem, the second type of variational region-based ACM namely the selective segmentation model is preferred. Selective segmentation involves dividing a specific object in an image into several sections using markers that are defined by the user. This method has a lot of potential for integration with medical imaging fields [18], [19] biometric identification [20] and processing of text [21]. Recently, Jumaat and Chen [22] proposed a prominent selective ACM namely the primal dual selective segmentation (PDSS). This model is proven efficient in segmenting a specific object in an input image. However, the PDSS model is facing a huge problem in segmenting images with low contrast. Due to the issue that arises, Ghani *et al.* [23] have proposed a modified PDSS model namely PDSS2 by substituting the fitting term with information from the image enhancement technique. However, the detailed information acquired by the PDSS2 seems to be insufficient to find the near-optimal segmented boundary of an object with intensity inhomogeneity problems. Recently in 2023, Saibin and Jumaat [24] proposed a new variational selective region-based ACM namely the Gaussian regularization selective segmentation (GRSS) model for intensity inhomogeneity images. However, the generated curve is not smooth because of the replacement of the total variation (TV) term with Gaussian kernel regularizer in the formulation.

Therefore, this paper proposes a new variational selective region-based ACM for images with intensity inhomogeneity by incorporating the ideas of using a saliency map from the SDREL model [17] and LSF model [16]. To integrate the local property of an input image, the idea from the LIF model [13] will be used. To capture a targeted, a distance function (DF) from the GRSS model [24] will be utilized. The remainder of this work is divided into three sections. In section 2 describes the study's method as well as the recommended energy functional of the proposed model. In section 3 contains a comparison and explanation of the experimental findings. The conclusion and recommendations for further study will be explored in section 4.

2. METHOD

The idea of formulating the new model is achieved by integrating the LSF model [16] into a variational minimization energy functional. To capture intensity inhomogeneity object, the LIF energy [13] is utilized. The method of the proposed model will be explained based on the flow chart in Figure 1 as follows. Based on Figure 1, the saliency map and LIF energy of an input image are computed. Next, the LSF energy is derived from the computed saliency map. After that, a total energy minimization functional that represent the new model is formulated to segment the input image by integrating the LSF and LIF energies with DF, distance regularization term (DRT) and length term, also known as TV function. In the next subsection, each step is explained in detail.

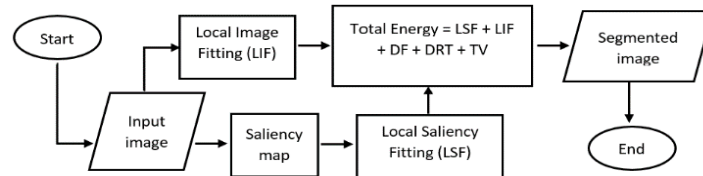


Figure 1. Flowchart of the proposed model

2.1. Input image

In this research, there will be five different categories of medical test images which are the mammogram, brain, ultrasound, chest X-rays and covid CT scan images taken from [25]–[29] respectively. There will be six different test images from each category will be segmented. Thus, a total of thirty images will be used in this study. The benchmarks for all the test images are taken from the same sources respectively.

2.2. Saliency map via absorbing markov chain

In our proposed model, saliency detection plays an important role. Unlike the classical saliency image map used in the LSF model [16], we propose to use the absorbing markov chain instead to compute the probability of a random walker being absorbed by different states in an image [30]. There are two different states involved which are the absorbing states, r and the transient states, t . The idea is that a state with high absorption probability represents a salient region in the image, as it attracts the random walker more than other states. These probabilities can be represented in the form of a matrix where matrix Q is the transition probabilities between the transient states, matrix R is the transition probabilities from transient to absorbing states and matrix I represents the identity matrix that describes the transition probabilities between the absorbing rates. Therefore, the transition matrix P can be defined in the form of;

$$P \rightarrow \begin{pmatrix} Q & R \\ 0 & I \end{pmatrix} \quad (1)$$

the method starts by constructing an image graph, where each node represents the super pixels and each edge connects two adjacent super pixels. The absorbed time for each transient state can be calculated as follows:

$$y = N \times c \quad (2)$$

here, the matrix c is the t -dimensional column vector whose elements are 1 and matrix N represents the fundamental matrix of the absorbing markov chain given by:

$$N = (I - Q)^{-1} \quad (3)$$

the transition matrix of the markov chain is then computed from this graph and the absorbing probability of each state is calculated using the theory of absorbing markov chains. The resulting probabilities are then used as the saliency map of the image and the absorbing state corresponds to the final saliency map and the transition probabilities between states are learned from the input image data which allows the algorithm to determine which regions are more salient. According to Jiang *et al.* [30], the saliency map S can be obtained by normalizing the absorbed time (2) and is given by:

$$S(i) = \bar{y}(i), \quad i = 1, 2, \dots, t \quad (4)$$

where i indicates the indexing of the transient nodes on a graph. This approach is effective in detecting salient regions in images and has been used in a variety of computer vision applications. To strengthen the claim,

we compared the classical saliency result obtained from the LSF model [16] with the saliency via absorbing markov chain [30] which is shown in Figure 2.

Based on Figure 2, the input image in Figure 2(a) is an intensity inhomogeneity synthetic image. From visual observation, we can see that the saliency detection using the classical method [16] in Figure 2(b) is less accurate to use in this study as it can produce a poorer salient image result as compared to the absorbing markov chain [30] in Figure 2(c). This is due to the advantages of the absorbing markov chain method on handling global and local saliency information as it defines absorbing states for important regions and adjusting transition probabilities accordingly.

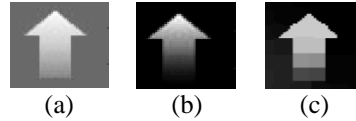


Figure 2. The input image with (a) its saliency map, (b) the classical saliency [16], and (c) the saliency via absorbing markov chain [30]

2.3. Local image fitting

In this study, the local image fitting is computed using the LIF model [13]. The local image fitting is important to handle images with intensity inhomogeneity. Assumed that for an image $u(x, y)$ in a domain Ω , the regularized local image fitting energy functional in the level set formulation E_ϵ^{LIF} is defined as follows:

$$E_\epsilon^{LIF}(\phi) = \frac{1}{2} \int_\Omega |u - u^{LIF}|^2 dx dy \tag{5}$$

where ϕ is the segmentation curve in zero-level set representation. The fitted image $u^{LIF} = u^{LIF}(x, y)$ in (5) can be written as follows:

$$u^{LIF} = n_1 H_\epsilon(\phi) + n_2 (1 - H_\epsilon(\phi)) \tag{6}$$

where n_1 and n_2 are the intensity averages of interior and exterior in a local region by defining a truncated Gaussian window $W_k(x, y)$ with a standard deviation σ and a radius κ of kernel window, which have the following definitions.

$$\begin{cases} n_1 = \text{mean} \left(u \in (\{(x, y) \in \Omega | \phi(x, y) > 0\} \cap W_k(x, y)) \right) \\ n_2 = \text{mean} \left(u \in (\{(x, y) \in \Omega | \phi(x, y) < 0\} \cap W_k(x, y)) \right) \end{cases} \tag{7}$$

In practical applications, the value of standard deviation σ is quite essential where it should be correctly selected based on the images. If the setting parameter σ is set to be small, it may provide incorrect results, whereas the σ value that is too large will result in a high computational cost. The heaviside function $H_\epsilon(\phi) = 0.5(1 + (2/\pi)\arctan(\phi/\epsilon))$ and the dirac delta function $\delta_\epsilon(\phi) = \epsilon/\pi(\epsilon^2 + \phi^2)$ are utilized in the model where ϵ is a small positive constant that handles the smoothness of $H_\epsilon(\phi)$ and $\delta_\epsilon(\phi)$ [24]. In this study, the epsilon parameter is set to $\epsilon = 1$.

2.4. Local saliency fitting

By combining (4) and (5), we proposed a new equation to compute the LSF as follows:

$$E_{LSF} = \frac{1}{2} \int_\Omega |S - S_{LSF}|^2 dx dy \tag{8}$$

where S is the saliency map equation obtained from (4) and S_{LSF} is the saliency-driven local fitted image defined as follows:

$$S_{LSF} = L_{s1}(x)H_\epsilon(\phi) + L_{s2}(x)(1 - H_\epsilon(\phi)) \tag{9}$$

here, the term L_1 and L_2 are the saliency-based intensity mean for the inside and outside of the contour as defined in (7) while H_ϵ is the heaviside function. The LSF enables the extraction of accurate local image information especially for images with inhomogeneous intensity to increase segmentation accuracy.

2.5. Total energy functional

In this step, a novel energy functional which is a new variational selective ACM called the saliency-based selective segmentation (SBSS) model is proposed. The proposed SBSS model consists of the combination of (5) and (8). In addition, to ensure the SBSS model capable to capture a specific object effectively, a $DF = \int_{\Omega} P_d H(\phi) dx dy$ is utilized. Here, P_d is the euclidean DF similarly defined in [24]. Moreover, a function $TV = \int_{\Omega} \delta(\phi) |\nabla \phi| dx dy$ is introduced to generate a smooth curve and a $DRT = \int_{\Omega} \frac{1}{2} (|\nabla \phi| - 1)^2 dx dy$ is also added in the SBSS model to stabilize the evolution of the generated segmentation contour. Thus, the variational energy functional minimization problem of the SBSS model in the level set formulation is defined as follows:

$$\begin{aligned} \min_{\phi} SBSS(\phi) = & \frac{1}{2} \int_{\Omega} \left[I - (m_1 H(\phi) + m_2 (1 - H(\phi))) \right]^2 dx dy + \theta \int_{\Omega} P_d H(\phi) dx dy \\ & + \frac{1}{2} \int_{\Omega} \left[S - (s_1 H(\phi) + s_2 (1 - H(\phi))) \right]^2 dx dy + \mu \int_{\Omega} \frac{1}{2} (|\nabla \phi| - 1)^2 dx dy + v \int_{\Omega} \delta(\phi) |\nabla \phi| dx dy \end{aligned} \quad (10)$$

here, the parameters θ, μ and v are positive integers to weight the DF, DRT, and TV functions respectively. To solve the model, the euler-lagrange partial differential equation is derived which is defined as the following (11).

$$\begin{aligned} \frac{\partial \phi}{\partial t} = & \delta(\phi) \left[I - (m_1 H(\phi) + m_2 (1 - H(\phi))) (m_1 - m_2) \right] - \mu \left(\Delta \phi - \nabla \cdot \frac{\nabla \phi}{|\nabla \phi|} \right) + \delta(\phi) (\theta P_d) \\ & + \delta(\phi) \left[S - (s_1 H(\phi) + s_2 (1 - H(\phi))) (s_1 - s_2) \right] - v \delta(\phi) \nabla \cdot \frac{\nabla \phi}{|\nabla \phi|} \end{aligned} \quad (11)$$

2.6. Algorithm to solve the SBSS model

To compute the solution of (11) that represents the euler-lagrange partial differential equation of the proposed SSBF model, MATLAB R2021a software was used. To stop the program automatically, two stopping criteria were utilized. Firstly, a tolerance value $tol = 1 \times 10^{-5}$ was defined and secondly, the maximum number of iterations, $maxit=200$ was used. Thus, the following Algorithm 1 outlines the process for implementing the new proposed SBSS model together with each respective MATLAB code.

Algorithm 1. For the SBSS model

1. Input the test image.
`>> Img = imread('image.png');`
2. Set values of tol , $maxit$, σ and θ .
`>> maxit = 200; tol=1e-5; theta=20; sigma =90;`
3. Marker set is defined around the targeted object.
`>> mx = [125;62;97;158;214;174]; my = [56;120;147;161;150;62];`
4. Evaluate the saliency map, S from Equation (4).
`>> SS=Saliency_MC_Lite(Img);`
5. For iteration=1 to $maxit$ or $\|\phi^{n+1} - \phi^n\|/\|\phi^n\| \leq tol$ do
 Generate the function ϕ which is the zero-level set function based on Equation (11).
`>> for iteration = 1: maxit`
`>> [phi]= SBSS (Img, SS, mx, my, theta, sigma, maxit, tol);`
`>> R=Residual (phi, oldphi)/norm(oldphi);`
`>> if R<tol, break, end`
`>> end`
`>> phi(phi>=0) =1; phi(phi<0) =0;`
6. The final segmentation curve will be the output ϕ .
`>> figure, imagesc(phi); colormap gray;`

3. RESULTS AND DISCUSSION

Throughout this investigation, the suggested SBSS model's performance was compared to the other three competing variational selective segmentation models: the PDSS model [23], the PDSS2 model [24], and the recently released GRSS model [25]. The accuracy of all models will be determined and computed using two similarity coefficients which are dice (DSC) and Jaccard (JSC) coefficients computation. The DSC and JSC coefficients are to be determined by the benchmark value of closest to 0 indicates the poorest quality while the value of closest to 1 indicates the nearly perfect segmentation result. In addition, the hausdorff distance (HD) measurement will be recorded as part of the accuracy test as it will determine the relative distance between the segmentation result and the ground truth contour. According to Isensee *et al.* [31], the lower the hausdorff distance value, the greater the similarity between the targeted object and the original ground truth image.

For every test image, the tolerance $tol = 1 \times 10^{-5}$ and the maximum iterations are 200. The parameters set in all the models have been adjusted thoroughly to obtain better segmentation results for each model. Then, the initial marker is defined and drawn relatively close to the targeted object in each image [32], [33]. The initial contour will then be self-generated where it combines all the markers to form a polygon [24]. After that, the parameter θ is set in the range of $\theta = [3, 17500]$. The value of the parameter θ varies according to the suitability of the image. The parameter ν is set in the range of $\nu = [10, 1500]$ while the parameter μ is fixed to $\mu = 0.001$. The segmentation results for all test images in each medical image's category by using the SBSS model and the other three models are compared and presented in Table 1.

Table 1. Segmentation results on different type of medical images

Test image	PDSS	PDSS2	GRSS	SBSS	Test image	PDSS	PDSS2	GRSS	SBSS
(1a)	(1b)	(1c)	(1d)	(1e)	(16a)	(16b)	(16c)	(16d)	(16e)
(2a)	(2b)	(2c)	(2d)	(2e)	(17a)	(17b)	(17c)	(17d)	(17e)
(3a)	(3b)	(3c)	(3d)	(3e)	(18a)	(18b)	(18c)	(18d)	(18e)
(4a)	(4b)	(4c)	(4d)	(4e)	(19a)	(19b)	(19c)	(19d)	(19e)
(5a)	(5b)	(5c)	(5d)	(5e)	(20a)	(20b)	(20c)	(20d)	(20e)
(6a)	(6b)	(6c)	(6d)	(6e)	(21a)	(21b)	(21c)	(21d)	(21e)
(7a)	(7b)	(7c)	(7d)	(7e)	(22a)	(22b)	(22c)	(22d)	(22e)
(8a)	(8b)	(8c)	(8d)	(8e)	(23a)	(23b)	(23c)	(23d)	(23e)
(9a)	(9b)	(9c)	(9d)	(9e)	(24a)	(24b)	(24c)	(24d)	(24e)
(10a)	(10b)	(10c)	(10d)	(10e)	(25a)	(25b)	(25c)	(25d)	(25e)
(11a)	(11b)	(11c)	(11d)	(11e)	(26a)	(26b)	(26c)	(26d)	(26e)
(12a)	(12b)	(12c)	(12d)	(12e)	(27a)	(27b)	(27c)	(27d)	(27e)
(13a)	(13b)	(13c)	(13d)	(13e)	(28a)	(28b)	(28c)	(28d)	(28e)
(14a)	(14b)	(14c)	(14d)	(14e)	(29a)	(29b)	(29c)	(29d)	(29e)
(15a)	(15b)	(15c)	(15d)	(15e)	(30a)	(30b)	(30c)	(30d)	(30e)

Table 1 demonstrates the comparison of segmentation results for all test images in each medical image's category by using the proposed SBSS model with the PDSS, PDSS2 and GRSS model. Tables 1(1a-6a) indicate six test mammogram images followed by brain images in Tables 1(7a-12a), ultrasound images in Tables 1(13a-18a), chest X-rays images in Tables 1(19a-24a) and the covid CT scan images in Tables 1(25a-30a). The yellow curve in Tables 1(1a-30a) indicated the initial contour for each ACMs. The results generated by the PDSS and PDSS2 models are demonstrated in Tables 1(1b-30b) and Tables 1(1c-30c) respectively. Tables 1(1d-30d) and Tables 1(1e-30e) show the results obtained by the GRSS and the proposed SBSS model respectively. By visual observation, it is clearly seen that all the models are capable to segment the targeted object for each respective image. However, the PDSS and PDSS2 models were over-segmented where the models were segmented with unnecessary noise and the generated curve become scattered simply because the model captured the targeted object together with the nearby area of the object boundary which happened to have the same intensity as per the targeted object. From the very closest point, it is clearly seen that the GRSS model also tends to segment image noise as observed in test images Table 1(25d) and Table 1(26d). In general, all the medical test images have different degrees of intensities together with weak boundaries which are difficult to be segmented. This is the main reason why the PDSS, PDSS2 and GRSS models are less effective.

On the other hand, the proposed SBSS model has produced a better segmentation result as compared to the PDSS, PDSS2, and GRSS models thanks to the absorbing markov chain-based saliency image map and the local image intensities respectively where the saliency image map assists the model in making the initial guess of the targeted object and the local image intensities idea is helps determine the sensitivity of the initial contour position and finding the near-optimal final contour, especially in segmenting images with intensity inhomogeneity and weak boundaries. To support the visual observations, the quantitative accuracy test for the SBSS model and the competing models is conducted. The results are tabulated in Table 2.

Table 2. The average hausdorff distance, average DSC, and average JSC values for all test images

Test image	Mammogram	Brain	Ultrasound	Chest	Covid	Average
PDSS	12.5625/	2.9327/	5.9503/	40.2790/	12.5131/	14.8475/
HD/DSC/JSC	0.9118/ 0.8399	0.9456/ 0.8971	0.8606/ 0.7650	0.7687/ 0.6283	0.4976/ 0.3481	0.7969/ 0.6597
PDSS2	12.5022/	2.8318/	6.1473/	42.4813/	12.4052/	15.2736/
HD/DSC/JSC	0.9164/ 0.8477	0.9467/ 0.8991	0.8927/ 0.8095	0.7698/ 0.6300	0.5036/ 0.3541	0.8058/ 0.7081
GRSS	13.0715/	2.9981/	4.0262/	19.3480/	10.0824/	9.9052/
HD/DSC/JSC	0.9007/ 0.8230	0.9421/ 0.8913	0.9443/ 0.8953	0.8351/ 0.7188	0.8655/ 0.7662	0.8975/ 0.8189
SBSS	11.1513/	2.6003/	3.0868/	13.5810/	9.4614/	7.9762/
HD/DSC/JSC	0.9340/ 0.8775	0.9522/ 0.9073	0.9551/ 0.9149	0.9166/ 0.8470	0.9255/ 0.8620	0.9367/ 0.8817

The average hausdorff distance, DSC and JSC values for all 30 medical test images were recorded as shown in Table 2. From Table 2, it is clearly shown that the SBSS model recorded the lowest average of hausdorff distance value of 7.9762 which is about 46.28%, 47.78%, and 19.47% lower than the PDSS, PDSS2 and GRSS models respectively. The SBSS model also recorded the highest average DSC and JSC values which are 0.9367 and 0.8817 respectively compared to the other models. This implies that the DSC values for the SBSS model are about 17.54%, 16.24%, and 4.37% higher than the PDSS, PDSS2, and GRSS models respectively, while the JSC values for the SBSS model are about 33.65%, 24.52%, and 7.67% higher than the PDSS, PDSS2, and GRSS models respectively. Thus, it can be concluded that the SBSS model is more accurate compared to the PDSS, PDSS2, and GRSS models. These are the evidence of the advantages of incorporating the absorbing markov chain saliency image detection and the local image fitting idea which help the SBSS model to handle images with intensity inhomogeneity that result in more accurate segmentation compared to the other competing models.

Even though it is proven visually and quantitatively that the SBSS model is more accurate than the PDSS, PDSS2, and GRSS models, the limitation of our proposed SBSS model is that it takes a longer processing time compared to the other models. The average processing time (in seconds) for all thirty tested medical images by using the PDSS, PDSS2, GRSS, and SBSS models is 45.8725s, 55.3803s, 48.7610s, and 77.5004s respectively. The time processing difference between the GRSS model and the SBSS model is because of the existence of the TV function in the SBSS model formulation which makes the formulation becomes more complicated, while the GRSS model replaced the TV regularization term with the gaussian kernel function which makes the GRSS model formulation less complicated resulting in less computational time. In addition, the SBSS model was solved using the gradient descent method, while the PDSS and PDSS2

models were solved using a fast-multilevel algorithm which is more efficient than the gradient descent method. Thus, on average the PDSS and PDSS2 models are more efficient than the SBSS model. Moreover, the implementation of the absorbing markov chain-based saliency image map detection, local image intensities and DRT term make the SBSS model's formulation more complex and it results in a significant increase in terms of computational time. Based on the experiment above, we remark that the proposed SBSS model is compared with three existing PDSS, PDSS2, and GRSS models where these three models do not involve saliency computation in their formulations. To complete our experiment, we compared our proposed model to the LSF model [16] that contains the saliency map. We selected three test images from [34] for this investigation, and the segmentation outcomes are compared in Figure 3.

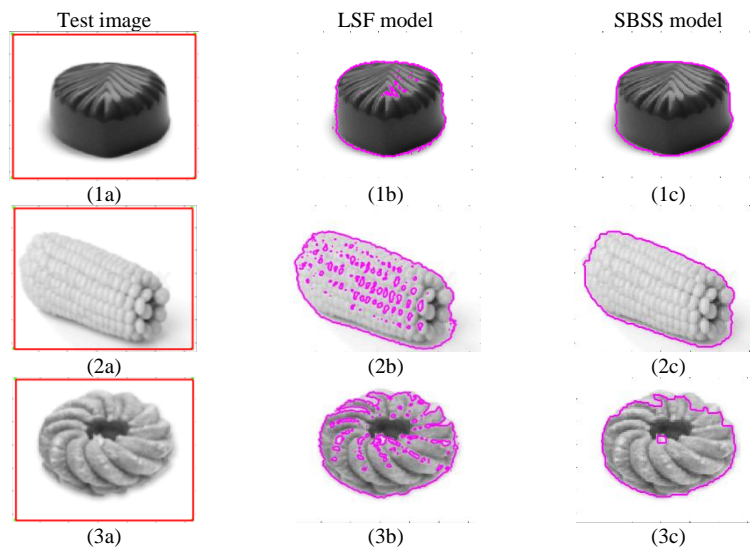


Figure 3. The input images, (1a) a chocolate, (2a) a corn, and (3a) a biscuit with their respective segmentation results (1b), (2b), and (3b) by using the LSF model and (1c), (2c), and (3c) the proposed SBSS model

From Figure 3, we present the segmentation output for the LSF model and the proposed SBSS model in the second and third columns, respectively. Meanwhile, the first column is the test image with the respective red initial contour in Figures 3(1a), 3(2a), and 3(3a). By visual observation, we can see that the segmentation results obtained from the LSF model in Figures 3(1b), 3(2b), and 3(3b) are scattered and produced unnecessary noise. On the other hand, the segmentation results produced by the proposed SBSS model in Figures 3(1c), 3(2c), and 3(3c) are smoother which makes the final contour becomes more accurate as compared to the LSF model, thanks to the absorbing markov chain formulation in the SBSS model formulation which assists in making a near-optimal initial guess and helps producing more accurate segmentation result.

Looking at the segmentation result visually is insufficient to judge the accuracy of a particular segmentation model. Hence, we present the quantitative accuracy measures using the average distance measures, DSC and JSC values for both models. As a result, the SBSS model recorded a lower hausdorff distance of 5.6431 compared to the LSF model with an average distance value of 5.9708. In addition, the average DSC and JSC values for the three test images recorded in the proposed SBSS model are 0.9468 and 0.8991, respectively, which are slightly higher than in the LSF model which are 0.9222 and 0.8565, respectively. Therefore, we can conclude that the SBSS model is more accurate compared to the LSF model. The better accuracy performance obtained from the proposed SBSS model are due to the advantages of applying the saliency image map which tends to produce primarily the nontrivial part of the image [35], incorporate specific features of human vision [36] and coherent initial guess via the absorbing markov chain and at the same time, enhances the overall visual quality of segmentation results.

4. CONCLUSION

In this study, a new variational selective region-based ACM for images with intensity inhomogeneity termed the SBSS model was introduced by integrating the idea of absorbing markov chain-based saliency image map detection and local image intensities. The respective euler-lagrange equation was provided to achieve the optimality of the image segmentation and was then solved in MATLAB. The performance of the proposed SBSS model with other existing models was evaluated based on segmentation accuracy and

efficiency. The segmentation accuracy was measured by the average hausdorff distance, DSC and JSC values, while the time processing was recorded to evaluate the segmentation efficiency. The results showed that all models could segment the targeted objects visually. However, the SBSS model had the highest accuracy, especially when dealing with segmenting images with intensity inhomogeneity even though the SBSS model took the longest execution time. In the near future, the model will be used in formulating a variational ACM for vector-valued images with intensity inhomogeneity and weak boundary problems.

ACKNOWLEDGEMENTS

Authors thank to GIP research grant (project's code: 600-RMC/GIP 5/3 (078/2022)), Universiti Teknologi MARA, Shah Alam for supporting this research. In addition, the APC was funded by Pembiayaan Yuran Penerbitan Artikel (PYPA), Tabung Dana Kecemerlangan Pendidikan (DKP), Universiti Teknologi MARA (UiTM), Malaysia.

REFERENCES

- [1] S. N. Kumar, A. L. Fred, H. A. Kumar, and P. S. Varghese, "Performance metric evaluation of segmentation algorithms for gold standard medical images," in *Advances in Intelligent Systems and Computing*, vol. 709, 2018, pp. 457–469.
- [2] S. S. Yasiran *et al.*, "Comparison between GVF snake and ED snake in segmenting microcalcifications," in *ICCAIE 2011 - 2011 IEEE Conference on Computer Applications and Industrial Electronics*, Dec. 2011, pp. 597–601, doi: 10.1109/ICCAIE.2011.6162204.
- [3] A. K. Jumaat, W. E. Z. W. A. Rahman, A. Ibrahim, and R. Mahmud, "Segmentation and characterization of masses in breast ultrasound images using active contour," in *2011 IEEE International Conference on Signal and Image Processing Applications, ICSIPA 2011*, Nov. 2011, pp. 404–409, doi: 10.1109/ICSIPA.2011.6144126.
- [4] S. S. Yasiran *et al.*, "Microcalcifications segmentation using three edge detection techniques," in *International Conference on Electronic Devices, Systems, and Applications*, Nov. 2012, pp. 207–211, doi: 10.1109/ICEDSA.2012.6507798.
- [5] A. K. Jumaat *et al.*, "Performance comparison of canny and sobel edge detectors on balloon snake in segmenting masses," in *2014 International Conference on Computer and Information Sciences, ICCOINS 2014 - A Conference of World Engineering, Science and Technology Congress, ESTCON 2014 - Proceedings*, Jun. 2014, pp. 1–5, doi: 10.1109/ICCOINS.2014.6868368.
- [6] M. Kass, A. Witkin, and D. Terzopoulos, "Snakes: active contour models," *International Journal of Computer Vision*, vol. 1, no. 4, pp. 321–331, Jan. 1988, doi: 10.1007/BF00133570.
- [7] S. Osher and J. A. Sethian, "Fronts propagating with curvature-dependent speed: algorithms based on Hamilton-Jacobi formulations," *Journal of Computational Physics*, vol. 79, no. 1, pp. 12–49, Nov. 1988, doi: 10.1016/0021-9991(88)90002-2.
- [8] H. Ali, L. Rada, and N. Badshah, "Image segmentation for intensity inhomogeneity in presence of high noise," *IEEE Transactions on Image Processing*, vol. 27, no. 8, pp. 3729–3738, Aug. 2018, doi: 10.1109/TIP.2018.2825101.
- [9] S. Soomro, A. Munir, and K. N. Choi, "Fuzzy c-means clustering based active contour model driven by edge scaled region information," *Expert Systems with Applications*, vol. 120, pp. 387–396, Apr. 2019, doi: 10.1016/j.eswa.2018.10.052.
- [10] D. Mumford and J. Shah, "Optimal approximations by piecewise smooth functions and associated variational problems," *Communications on Pure and Applied Mathematics*, vol. 42, no. 5, pp. 577–685, Jul. 1989, doi: 10.1002/cpa.3160420503.
- [11] T. F. Chan and L. A. Vese, "Active contours without edges," *IEEE Transactions on Image Processing*, vol. 10, no. 2, pp. 266–277, 2001, doi: 10.1109/83.902291.
- [12] C. Li, C. Y. Kao, J. C. Gore, and Z. Ding, "Implicit active contours driven by local binary fitting energy," in *Proceedings of the IEEE Computer Society Conference on Computer Vision and Pattern Recognition*, Jun. 2007, pp. 1–7, doi: 10.1109/CVPR.2007.383014.
- [13] K. Zhang, H. Song, and L. Zhang, "Active contours driven by local image fitting energy," *Pattern Recognition*, vol. 43, no. 4, pp. 1199–1206, Apr. 2010, doi: 10.1016/j.patcog.2009.10.010.
- [14] H. Wang and T. Z. Huang, "An adaptive weighting parameter estimation between local and global intensity fitting energy for image segmentation," *Communications in Nonlinear Science and Numerical Simulation*, vol. 19, no. 9, pp. 3098–3105, Sep. 2014, doi: 10.1016/j.cnsns.2014.02.015.
- [15] Y. Yang, W. Jia, and B. Wu, "Simultaneous segmentation and correction model for color medical and natural images with intensity inhomogeneity," *Visual Computer*, vol. 36, no. 4, pp. 717–731, Apr. 2020, doi: 10.1007/s00371-019-01651-4.
- [16] E. Iqbal, A. Niaz, A. A. Memon, U. Asim, and K. N. Choi, "Saliency-driven active contour model for image segmentation," *IEEE Access*, vol. 8, pp. 208978–208991, 2020, doi: 10.1109/ACCESS.2020.3038945.
- [17] X. H. Zhi and H. Shen, "Saliency driven region-edge-based top down level set evolution reveals the asynchronous focus in image segmentation," *Pattern Recognition*, vol. 80, pp. 241–255, 2018, doi: 10.1016/j.patcog.2018.03.010.
- [18] N. F. Idris, M. A. Ismail, M. S. Mohamad, S. Kasim, Z. Zakaria, and T. Sutikno, "Breast cancer disease classification using fuzzy-ID3 algorithm based on association function," *IAES International Journal of Artificial Intelligence*, vol. 11, no. 2, pp. 448–461, Jun. 2022, doi: 10.11591/ijai.v11.i2.pp448-461.
- [19] H. M. Ahmed and M. Y. Kashmola, "A proposed architecture for convolutional neural networks to detect skin cancers," *IAES International Journal of Artificial Intelligence*, vol. 11, no. 2, pp. 485–493, 2022, doi: 10.11591/ijai.v11.i2.pp485-493.
- [20] A. H. T. Al-Ghrai, A. A. Mohammed, and E. Z. Sameen, "Face detection and recognition with 180 degree rotation based on principal component analysis algorithm," *IAES International Journal of Artificial Intelligence*, vol. 11, no. 2, pp. 593–602, Jun. 2022, doi: 10.11591/ijai.v11.i2.pp593-602.
- [21] M. Z. Ansari, T. Ahmad, M. M. S. Beg, and N. Bari, "Language lexicons for Hindi-English multilingual text processing," *IAES International Journal of Artificial Intelligence*, vol. 11, no. 2, pp. 641–648, 2022, doi: 10.11591/ijai.v11.i2.pp641-648.
- [22] A. K. Jumaat and K. Chen, "A reformulated convex and selective variational image segmentation model and its fast multilevel algorithm," *Numerical Mathematics*, vol. 12, no. 2, pp. 403–437, Jun. 2019, doi: 10.4208/nmtma.OA-2017-0143.
- [23] N. A. S. M. Ghani, A. K. Jumaat, and R. Mahmud, "Boundary extraction of abnormality region in breast mammography image using active contours," *ESTEEM Academic Journal*, vol. 18, pp. 115–127, 2022.

- [24] T. C. Saibin and A. K. Jumaat, "Variational selective segmentation model for intensity inhomogeneous image," *Indonesian Journal of Electrical Engineering and Computer Science (IJECS)*, vol. 29, no. 1, pp. 277–285, Jan. 2023, doi: 10.11591/ijeecs.v29.i1.pp277-285.
- [25] I. C. Moreira, I. Amaral, I. Domingues, A. Cardoso, M. J. Cardoso, and J. S. Cardoso, "INbreast: toward a full-field digital mammographic database.," *Academic Radiology*, vol. 19, no. 2, pp. 236–248, Feb. 2012, doi: 10.1016/j.acra.2011.09.014.
- [26] J. Cheng, "brain tumor dataset (Version 5)," *Figshare*. 2017, doi: 10.6084/m9.figshare.1512427.v5.
- [27] A. Rodtook, K. Kirimasthong, W. Lohitvisate, and S. S. Makhanov, "Automatic initialization of active contours and level set method in ultrasound images of breast abnormalities," *Pattern Recognition*, vol. 79, pp. 172–182, Jul. 2018, doi: 10.1016/j.patcog.2018.01.032.
- [28] S. Candemir *et al.*, "Lung segmentation in chest radiographs using anatomical atlases with nonrigid registration," *IEEE Transactions on Medical Imaging*, vol. 33, no. 2, pp. 577–590, Feb. 2014, doi: 10.1109/TMI.2013.2290491.
- [29] S. P. Morozov *et al.*, "MosMedData: Chest CT Scans With COVID-19 related findings dataset," arXiv preprint arXiv, 2020.
- [30] B. Jiang, L. Zhang, H. Lu, C. Yang, and M. H. Yang, "Saliency detection via absorbing markov chain," in *Proceedings of the IEEE International Conference on Computer Vision*, 2013, pp. 1665–1672, doi: 10.1109/ICCV.2013.209.
- [31] F. Isensee *et al.*, "Automated brain extraction of multisequence MRI using artificial neural networks," *Human Brain Mapping*, vol. 40, no. 17, pp. 4952–4964, 2019, doi: 10.1002/hbm.24750.
- [32] A. K. Jumaat and K. Chen, "Three-dimensional convex and selective variational image segmentation model," *Malaysian Journal of Mathematical Sciences*, vol. 14, no. 3, pp. 437–450, 2020.
- [33] A. K. Jumaat and K. Chen, "An optimization-based multilevel algorithm for variational image segmentation models," *Electronic Transactions on Numerical Analysis*, vol. 46, pp. 474–504, 2017.
- [34] M. Y. Chen *et al.*, "Automatic Chinese food identification and quantity estimation," in *SIGGRAPH Asia 2012 Technical Briefs, SA 2012*, Nov. 2012, pp. 1–4, doi: 10.1145/2407746.2407775.
- [35] P. T. Krishnan, P. Balasubramanian, V. Jeyakumar, S. Mahadevan, and A. N. J. Raj, "Intensity matching through saliency maps for thermal and visible image registration for face detection applications," *Visual Computer*, 2022, doi: 10.1007/s00371-022-02605-z.
- [36] V. Lukin, E. Bataeva, and S. Abramov, "Saliency map in image visual quality assessment and processing," *Radioelectronic and Computer Systems*, no. 1–105, pp. 112–121, Mar. 2023, doi: 10.32620/reks.2023.1.09.

BIOGRAPHIES OF AUTHORS



Muhammad Syukri Mazlin    received his B.Sc. Degree in Mathematics from Universiti Teknologi MARA (UiTM) Shah Alam. His research interests include mathematical modeling and image processing. Currently, he is studying M.Sc. degrees in Mathematics at School of Mathematical Sciences, College of Computing, Informatics and Mathematics, UiTM in mathematical imaging techniques. He can be contacted at email: syukri.work03@gmail.com.



Abdul Kadir Jumaat    received the B.Sc. and M.Sc. Degrees in Mathematics from the Universiti Teknologi MARA, (UiTM) Shah Alam, Malaysia and the Ph.D. degree in Applied Mathematics (Mathematical Imaging Methods) from the University of Liverpool, United Kingdom. He is now serving as a senior lecturer at the School of Mathematical Sciences, College of Computing, Informatics and Mathematics and a research fellow at the Institute for Big Data Analytics and Artificial Intelligence (IBDAAI) in UiTM Shah Alam, Malaysia. His research interests include image/signal processing, artificial intelligence, computer vision, biometrics, medical image and analysis, and pattern recognition. He can be contacted at email: abdulcadir@tmsk.uitm.edu.my.



Rohana Embong    received the B.Sc. Degree in Mathematics from Iowa State University, Iowa, United States of America dan the M. Sc in Pure Mathematics from UMIST and the Victoria University of Manchester, Manchester, United Kingdom. She is an Associate Professor at the School of Mathematical Sciences, College of Computing, Informatics and Mathematics, UiTM Shah Alam, Malaysia. Her research interests include image processing and fuzzy mathematics. She can be contacted at rohana@fskm.uitm.edu.my.